IOP Publishing Journal of Physics D: Applied Physics

J. Phys. D: Appl. Phys. **55** (2022) 475101 (12pp) https://doi.org/10.1088/1361-6463/ac928a

# E-shaped patch antenna for GaAs-based broadband THz detectors

**X R Lian**[1], **K Wang**[2], **X Q Bai**[1], **P Bai**[3], **X H Li**[1], **S H Huang**[1], **W J Song**[1], **W Z Shen**[1], **G Y Xu**[2,4,*] and **Y H Zhang**[1,*]

[1] Key Laboratory of Artificial Structures and Quantum Control, School of Physics and Astronomy, Shanghai Jiao Tong University, Shanghai 200240, People's Republic of China
[2] Key Laboratory of Infrared Imaging Materials and Detectors, Shanghai Institute of Technical Physics, Chinese Academy of Sciences, Shanghai 200083, People's Republic of China
[3] Institute of Applied Physics and Computational Mathematics, Beijing 100088, People's Republic of China
[4] Hangzhou Institute for Advanced Study, University of Chinese Academy of Sciences, Hangzhou 310024, People's Republic of China

E-mail: yuehzhang@sjtu.edu.cn and gangyi.xu@mail.sitp.ac.cn

Received 23 June 2022, revised 5 September 2022
Accepted for publication 16 September 2022
Published 30 September 2022

## Abstract

High-performance broadband terahertz (THz) photodetectors are of great interest driven by lots of applications. To improve the performance of the THz photodetector in a wide spectral coverage, the E-shaped patch antenna with three slots is proposed and studied in theory. GaAs-based homojunction interfacial work function internal photoemission (HIWIP) broadband THz detector is used as an example to demonstrate the effect in broadband detection. Due to the combined effect of the antenna and the microcavity, E-shaped patch antenna microcavity HIWIP increase the optical coupling efficiency in a broadband range from 2.1–20 THz by an average of four times. Considering the requirement to reduce the dark current, the etched E-shaped patch antenna microcavity HIWIP only retaining the active region beneath the antenna is further investigated. In contrast to the reference HIWIP, the coupling efficiency is improved by an average of 15 times in 2.3–20 THz. The high coupling efficiency of both structures leads to the significant improvement of the responsivity, noise equivalent power, and detectivity in a wide spectral coverage theoretically, which makes it possible to realize higher operating temperatures. Such a design scheme of E-shaped patch antenna structure provides a guideline for broadband THz detectors and can be used for other THz detectors.

Keywords: terahertz photodetector, broadband detection, E-shaped patch antenna, etched E-shaped patch antenna, optical coupling efficiency

(Some figures may appear in colour only in the online journal)

## 1. Introduction

Terahertz (THz) detection is widely used in medicine, security, communication, astronomy, and biological detection [1–3]. There has been a lot of research on THz detectors over the years. Driven by vast potential applications, broadband THz detectors attract more and more attention because they can obtain more information and are a crucial part of THz multicolor imaging and up-converter [4, 5]. High-performance broadband THz detectors covering 1–10 THz are especially of great interest and is critically required for most application. At present, such detectors encounter different difficulties. THz broadband detectors based on thermal effect, such as the Golay Cell and bolometer, are limited by slow response speed [6, 7]. Blocked-impurity-band (BIB) detectors

---

[*] Authors to whom any correspondence should be addressed.

used for 1–15 THz face the problem of high purity requirement, passivation, and reproducibility [8, 9]. In recent years, two-dimensional materials have attracted broad attention in broadband detector studies. Graphene, as a representative 2D material, is one of the most commonly used materials for achieving broadband detection [10, 11]. Graphene materials are designed to achieve tunable THz absorption [12]. The antenna-integrated graphene p-n junction photodetector can achieve detection from 1.8–4.2 THz [11]. An ultra-broadband detection at room temperature using carbon nanotubes is reported [13]. Black phosphorus-based photoconductors show a high-performance in ultra-broadband detection from the infrared to THz frequencies [14]. Although broadband detectors based on 2D-materials demonstrate high performance, the material growth and device fabrication are technically less mature. Limitations in mass manufacturing and integration with existing readout circuits remain to be the primary barriers for the widespread.

GaAs-based homojunction\heterojunction interfacial work function internal photoemission (HIWIP\HEIWIP) detectors are noticed for the mature growth and manufacturing process, wide detection range, tailorable cutoff frequency, convenience to fabricate, and high response speed [15–18]. The spectral coverage of the HIWIP\HEIWIP detector spans from THz to infrared and the cutoff frequency in the THz band could be down to 1 THz [18]. Though the ultra-broadband detection of such kind of detector is of great interest, progress has been impeded by two obstacles. One is the relatively low responsivity in the low THz range, e.g. at 2–5 THz, where the high-performance THz source (THz QCL) usually operates and is critically required for most of the applications [16]. Another disadvantage is that the operating temperature of HIWIP requires to be around liquid helium temperature. To improve the responsivity and operation temperature, researchers are devoted to optimizing the structure parameters of the IWIP detector itself as possible. However, due to the limitation of doping concentration, significant improvement is difficult to be developed. Generally, enhancing the effective optical coupling is assumed to be a favorable alternative to improve the detectivity and responsivity, which has the potential to increase the operating temperature either [19, 20]. It has been proved that the coupling efficiency of THz photodetectors can be improved by metal structures such as gratings [21–23] and antennas [24, 25]. However, such conventional optical structures usually enhance in a narrow band and are not suitable for broadband detectors. In the microwave band, there have been many studies on how to use patch antennas for broadband enhancement. One simple method is to change the shape of the patch antenna. U-slotted [26, 27], E-shaped [28, 29], and other antenna shapes are used in the microwave field to achieve a wider range of responses. The stacked patch antenna structure can also achieve broadband enhancement [30], which requires adding a layer of patch antennas in the center of the dielectric layer. Adding a parasitic patch antenna is another way to broaden the band [31]. The main idea of the above method is to generate more resonant mode. In the THz metamaterial absorber, the rectangular resonator with an elongated slot as a perfect metamaterial absorber shows an absorption range from 1.24–2.58 THz [32]. But its band range is far from meeting the requirements of broadband detectors. How to achieve optical coupling enhancement in the low frequency THz band by antenna design has an important impact on improving the responsivity of broadband detectors. Through comparative studies among C-shaped, U-slotted, and E-shaped patch antenna in the microwave band, the E-shaped antenna is ideal for broad-spectrum [33]. In addition, an E-shaped patch antenna can achieve a broadband effect with only one unit, indicating the simplicity of fabrication and facility of integration.

In this paper, the E-shaped patch antenna (a square patch with three slots) is studied theoretically to improve the performance of a broadband THz detector. GaAs-based HIWIP is selected as an example to demonstrate the effect of the E-shaped patch antenna on the performance improvement in a wide THz band. By exciting multiple resonant modes, the E-shaped patch antenna can achieve broadband optical coupling enhancement. Compared with HIWIP, E-shaped antenna microcavity HIWIP (EAM-HIWIP) improves the coupling efficiency by an average of four times due to the combined effect of the antenna effect and the microcavity coupling effect. To further reduce the dark current, the etched EAM-HIWIP (EEAM-HIWIP) was investigated by removing away the active region except for the position beneath the E-shaped patch antenna. In addition to the capability of reducing the dark current, the coupling efficiency is improved by an average of four times compared to EAM-HIWIP. EAM-HIWIP and EEAM-HIWIP can not only improve the responsivity, the noise equivalent power (NEP), and detectivity in broadband significantly but also has the potential to improve the operating temperature, leading to a good prospect in THz broadband detection and multicolor imaging. The design of an E-shaped patch antenna provides a guideline to other broadband THz detectors, e.g. HEIWIP and BIB.

## 2. Methods

p-GaAs HIWIP device is chosen as the reference device [16]. Figure 1(a) shows the schematic structure of a HIWIP. It is composed of multi-layer structures in which an undoped GaAs intrinsic layer and a highly doped GaAs emitter layer are periodically stacked [34]. The detection mechanism involves three steps, which are shown in figure 1(b) by the energy band diagram. Firstly, the incident light is absorbed in the highly doped emitter layers mainly by free carrier absorption. Subsequently, the photo-excited carriers transport to the emitter/intrinsic interface through inelastic scattering progress. Finally, the carriers pass across the interface barrier and are collected under the electric field. Therefore, the quantum efficiency $\eta_q = \eta_a \eta_b \eta_c$, $\eta_a$ is the effective absorption efficiency (the ratio of the number of absorbed photons to that of the incident photons) which is closely dependent on the optical coupling efficiency $\eta$ and the absorption probability of material $A$, $\eta_b$ is the internal photoemission efficiency, $\eta_c$ is the collection

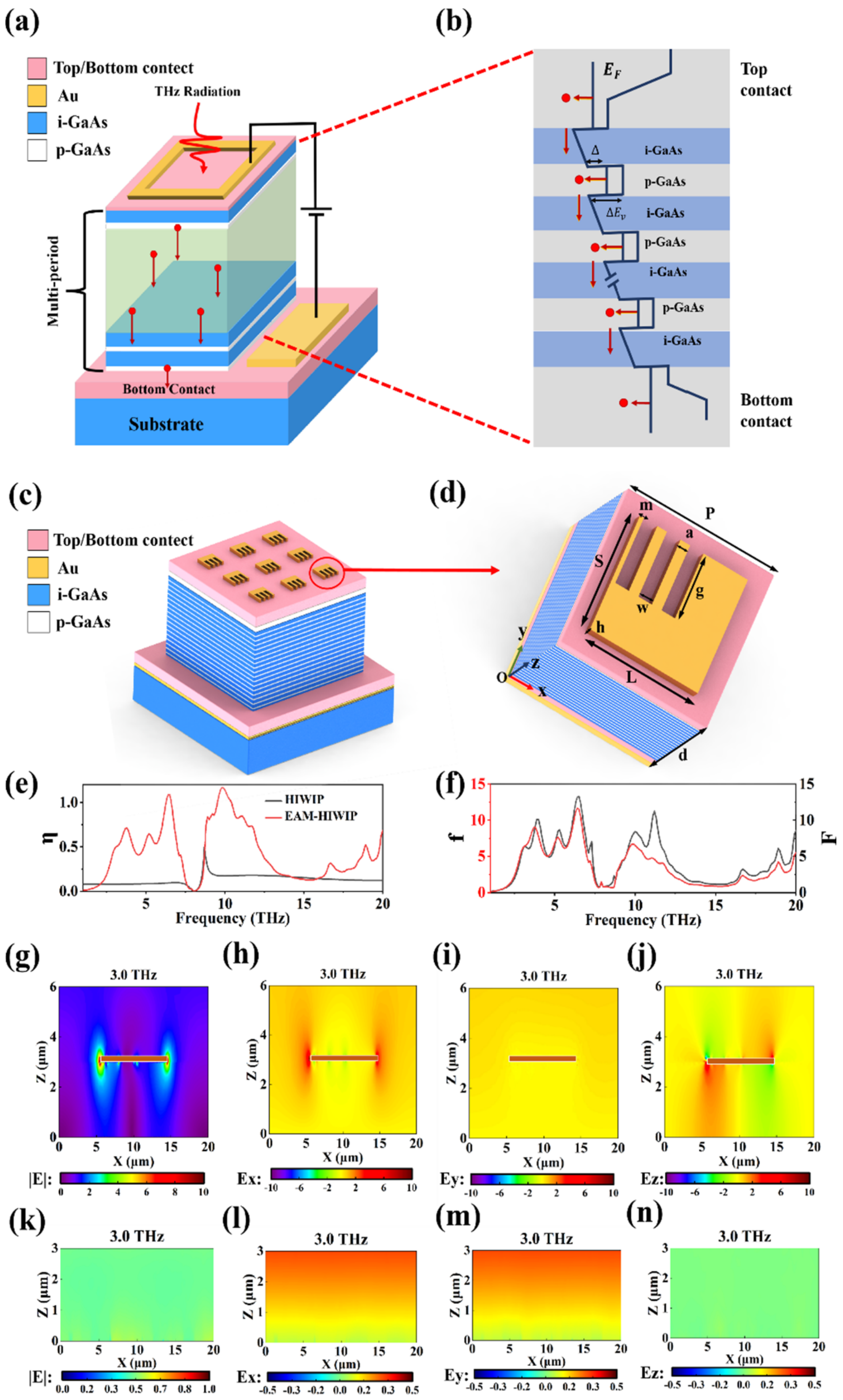

**Figure 1.** (a) The structural diagram of p-GaAs HIWIP detector. (b) The schematic energy band diagram of p-GaAs HIWIP. (c) The schematic device structure of EAM-HIWIP. (d) The schematic diagram of one unit cell in the E-shaped patch antenna array. (e) The coupling efficiency of HIWIP and EAM-HIWIP. (f) The enhancement factor of coupling efficiency f and the enhancement factor of the effective absorption efficiency F for EAM-HIWIP. The electric field distribution of EAM-HIWIP at 3.0 THz in the $x$–$z$ plane at $y = 10$ $\mu$m (g) |E|, (h) $E_x$, (i) $E_y$, (j) $E_z$, when $a = 1.5$ $\mu$m, $w = 0.5$ $\mu$m, $g = 5$ $\mu$m, $h = 100$ nm, $S = 9$ $\mu$m, $P = 20$ $\mu$m and $d = 3$ $\mu$m. (k)–(n) The corresponding electric distribution of HIWIP at 3.0 THz in the $x$–$z$ plane.

efficiency [16, 35]. The responsivity $R=\frac{q\eta_q\lambda}{hc}$, $q$ is the charge, $\lambda$ is the wavelength, $h$ is the Planck constant, $c$ is the speed of light in vacuum [36]. The relationship between responsivity and quantum efficiency shows that the enhancement of the quantum efficiency is helpful to increase the responsivity of the device. It is known that high quantum efficiency can be acquired either by enhancing the effective photon absorption or by improving the internal photoemission and collection probability of carriers. For a given structure, the internal photoemission and collection probability of carriers are almost determined. The most likely way to improve the performance is to increase the absorption in the active layer as high as possible. Generally, there are two kinds of effective ways to enhance the photon absorption. One is to utilize high doping concentration to increase the intrinsic free carrier absorption of the emitter layer, the other is to design a suitable optical coupling structure. By introducing the patch antenna microcavity coupling structure, the distribution of the optical electric field inside the active region is optimized and more light is coupled into the active region of the device. The coupling efficiency $\eta$ is enhanced significantly, leading to the effective photon absorption $\eta_a$ increases and thus effectively improving the quantum efficiency. It should be noted that the carrier distribution in the emitter layer is three-dimensional due to the high doping concentration and the thickness of the emitter layer similar to the scatting length [37]. The absorption mechanism based on free carrier absorption is different from that of intersubband transition involved in n-type quantum well photodetectors, leading to the fact that HIWIP responds to incident light without polarization selection. Though the photo-excited carriers contributing to photocurrent should fall in the escape cone with momentum normal to the emitter/intrinsic interface, such an effect has already been considered in $\eta_b$. Therefore, it is reasonable to assume that the responsivity could be improved by adopting an optical coupling structure. Considering the effect of optical coupling efficiency in a broadband range and the need for an easy-made process, different optical coupling schemes are compared and an E-shaped patch antenna array with a metal mirror at the bottom of the active region is adopted in the end. The schematic structure is shown in figure 1(c). The detailed structure of one period in EAM-HIWIP is zoomed in as shown in figure 1(d). The top layer is an E-shaped patch antenna, the middle layer is the active region of the detector, and the bottom layer is a metal mirror. Different from the square patch antenna, the optimized E-shaped antenna structure adds three slots based on the square. The width, the length, the distance between each slot, and the distance from the first slot to the left antenna edge are $w$, $g$, $a$, and $m$, respectively. The parameters $L$, $S$, and $P$, represent the length, width, and period of the entire E-shaped patch antenna. The variable $d$ is the thickness of the active region. The origin point is labeled in figure 1(d) and $z=0$ $\mu$m denotes the interface of the active region and the bottom metal layer.

COMSOL Multiphysics based on the finite element method is used in this simulation. The same boundary condition settings are used to ensure the accuracy of simulation in the three structures we calculated: the reference detector without the antenna structure (HIWIP), the EAM-HIWIP, and the EEAM-HIWIP. For these three structures, light is incident on the surface of the structure along the normal line and is set as the first order plane wave. $E_{0x}$ and $E_{0y}$ are the x and y component of the incident electric field, and is set to be unit magnitude of 1 V m$^{-1}$, which actually indicates the 45-degree polarization. Because the HIWIP can absorb light in all directions, the electric fields are presented in the $x$, $y$, and $z$ directions. We set continued periodic conditions along both the $x$ and $y$ directions. The patch and the bottom metal mirror are set to be gold with a thickness of $h=100\,nm$. The concerned dielectric function, the refractive index and the extinction coefficient of the metal Au is given by COMSOL according to the Drude model.

To study the enhancement effect of E-shaped patch antenna on GaAs-based broadband detectors, HIWIP in [16] with a thickness of 3 $\mu$m is selected as the benchmark. According to the effective dielectric model [38], the overall active region with multiple periods of intrinsic/emitter layers could be approximately equivalent to a unified doped GaAs layer for simplicity. The dielectric function for GaAs is calculated using a classical dielectric equation for damped harmonic oscillators and the Drude model [34]:

$$\varepsilon(\omega)=\varepsilon_\infty\left[1-\frac{\omega_p^2}{\omega(\omega+i\omega_0)}\right]+\frac{\omega_{TO}^2(\varepsilon_s-\varepsilon_\infty)}{\omega_{TO}^2-\omega^2-i\omega\gamma} \quad (1)$$

$$\omega_p=\sqrt{\frac{N_d q^2}{\varepsilon_0\varepsilon_s m_e^*}}. \quad (2)$$

The first term in the right of equation (1) means the free carrier absorption, $\omega_p$is the plasma frequency. The related parameters were given in [34]. Based on the conventional definition of the coupling efficiency of photodetectors, we use the volume-averaged $|E|^2$ to measure the coupling efficiency [24, 39, 40]:

$$\eta=\frac{\iiint_{V_{AR}}|E|^2dv}{\iiint|E_0|^2dv} \quad (3)$$

where $V_{AR}$ is the volume of the active region, $E$ is the averaged electric field in the active region, and $E_0$ is the averaged electric field of incident light. To demonstrate the broadband enhancement effect of the E-shaped patch antenna, the enhancement factor of the coupling efficiency $f$ is defined:

$$f=\frac{\eta_{EAM(EEAM)}}{\eta_{HIWIP}} \quad (4)$$

where $\eta_{EAM(EEAM)}$ and $\eta_{HIWIP}$ is the coupling efficiency of EAM/EEAM-HIWIP and HIWIP, respectively. The enhancement factor of the effective absorption efficiency $F$ is defined:

$$F=\frac{\eta_{a-EAM(EEAM)}}{\eta_{a-HIWIP}} \quad (5)$$

where $\eta_{a-EAM(EEAM)}$ and $\eta_{a-HIWIP}$ is the effective absorption efficiency $\eta_a$ of EAM/EEAM-HIWIP and HIWIP, respectively.

Figure 1(e) shows the comparison of the coupling efficiency $\eta$ of HIWIP and EAM-HIWIP. As revealed in figure 1(e), the coupling efficiency of HIWIP is very low in a wide range. The coupling efficiency is around 0.08 in 1–7.3 THz and 0.17 in 9.1–20 THz. The peak at 8.7 THz corresponds to the phonon-polariton state [25]. In contrast, the coupling efficiency of the EAM-HIWIP improved nearly four times on average in a wide spectral range from 2.1–20 THz, showing an excellent broadband enhancement ability. It is noted that the coupling efficiency is enhanced significantly in the low THz frequency range of 2.1–12 THz where more concerns are paid. Four coupling peaks can be observed at 3.0, 3.8, 5.2, and 6.4 THz. The valley in 7.4–8.3 THz corresponds to the GaAs Reststrahlen band which is due to the interaction between the incident electromagnetic field and the transverse optical phonons [24]. The improvement of the coupling efficiency due to the E-shaped antenna leads to a significant increase in the effective absorption efficiency, as shown in figure 1(f). It indicates that for a given detector, increasing the coupling efficiency is an effective way to improve the absorption in the detector. Therefore, we will focus on the discussion of the coupling efficiency in the following. In order to clarify the reason of enhancement, the electric field distribution of $E_x$ and $E_y$, and $E_z$ under the E-shaped patch antenna with $S = L = 9$ $\mu$m, $P = 20$ $\mu$m and $d = 3$ $\mu$m in the cross-section $x$–$z$ plane along $y = 10$ $\mu$m at the coupling peaks (3.0, 3.8, 5.2 and 6.4 THz) are studied carefully. At these four coupling frequencies, the electric field distribution characteristic of each component shows similarities. To simplify, figures 1(g)–(j) shows the electric field component for the first peak at 3.0 THz as an example. The corresponding electric field distribution for HIWIP at 3.0 THz is shown in figures 1(k)–(n) either for comparison. It can be seen that the $E_z$ component of HIWIP is almost zero compared with $E_x$ and $E_y$, and $E_z$ is significantly improved after adding the antenna microcavity structure. Comparing (j) and (n), it can be concluded that the electric field is mainly enhanced in the $E_z$ component. In EAM-HIWIP, the coupling enhancement is mainly due to the microcavity effect in $E_z$. Therefore, we will focus on $|E_z|$ in the following discussion.

## 3. Results and discussion

### 3.1. EAM-HIWIP

To investigate the effect of the structure parameters of E-shaped patch antenna microcavity on the coupling efficiency, the preliminary size of the microcavity should be given. When designing the antenna size, the threshold frequency of the device should be considered. In terms of the threshold frequency of HIWIP and HEIWIP (3–4 THz) [4, 41], we chose $S = L = 9$ $\mu$m for the first order resonance ($TM_{01}/TM_{10}$) around 3–4 THz using the equation

$$V_{NM} = \frac{c}{2n_{eff}S}\sqrt{N^2 + M^2} \tag{6}$$

where $N$, $M$ is the order of the TM mode under the patch, $V_{NM}$ is the resonance frequency of the TM mode, $S$ is the width of the patch antenna, and $n_{eff}$ is the effective refractive index [42]. The numerical study in grating shows that the duty cycle is optimized at 50% [43], so the period $P$ is approximately chosen for 20 $\mu$m. Figure 1(e) gives the coupling efficiency of the E-shaped patch antenna microcavity structure with $S = L = 9$ $\mu$m, $P = 20$ $\mu$m, $w = 0.5$ $\mu$m, $g = 5$ $\mu$m, $a = 1.5$ $\mu$m, and $d = 3$ $\mu$m. In a wide spectral range from 1–20 THz, such E-shaped patch antenna microcavity demonstrates obvious improvement.

The reason why an E-shaped patch antenna can exhibit a broadband coupling enhancement is shown in figure 2. Due to the difference in the effective refractive index of the single metal region and double metal region, an impedance mismatch is created, forming a standing wave under the metal patch [44]. The electric field distribution under the patch antenna satisfies:

$$E_z(x, y) \approx E_z \cos\left(\frac{\pi N}{s}x\right) sin\left(\frac{\pi M}{s}y\right). \tag{7}$$

The electric field distribution can be used to determine the mode of each resonance frequency. Because the dispersion curve of GaAs split into two branches in the THz range, i.e. the upper polariton branch and lower polariton branch, which means there will be two frequencies for each wavenumber $k$ for EM mode inside the structure [44]. The cavity mode which has the same mode number below and above the Reststrahlen band has the same electric field distribution. Therefore, we only focus on the discussion of the four peaks below the Reststrahlen band in figure 1(e), because the peaks above the Reststrahlen band could be understood in the same way. Figure 2 shows the electric field distribution of four peaks at 3.0 THz, 3.8 THz, 5.2 THz, 6.4 THz, figures 2(a), (c), (e) and (i) show |E| in $x$–$y$ plane at $z = 2$ $\mu$m, figures 2(b), (d), (g), (h) and (j) show $|E_z|$ in the $x$–$z\backslash y$–$z$ plane along the yellow dotted line. At 3.0 THz, the electric field |E| in the $x$–$y$ plane is mainly distributed at the right and left side of the patch in the $y$-direction and a first-order resonance mode in the $x$-direction is observed in figure 2(b). The transformation from the standard TM electric field of a patch antenna results from the effect of three slots. In contrast, at 3.8 THz, the electric field |E| localized around the top and bottom of the patch along the $x$-direction in figure 2(c) and a first-order resonance mode in the $y$-direction can be seen in figure 2(d). It should be noted that for a regular square patch antenna with the same size the first-order resonance mode along $x$-direction and $y$-direction degenerated at 3.8 THz. Due to the presence of three slots, such two resonance modes split and the one along the $x$-direction moves to 3.0 THz, leading to the broadening in low THz frequency.

The |E| and $|E_z|$ of the third peak at 5.2 THz are shown in figures 2(e), (g) and (h). It can be seen in figure 2(e) that the electric field |E| roughly concentrated on four zones of the patch. Considering the asymmetric geometry, the E-shaped patch antenna can be looked upon as left and right parts divided by the red line or the top and bottom parts divided by the blue line, as shown in figure 2(f). It is meaningful to inspect the electric field $|E_z|$ distribution of each part. Figure 2(g) is

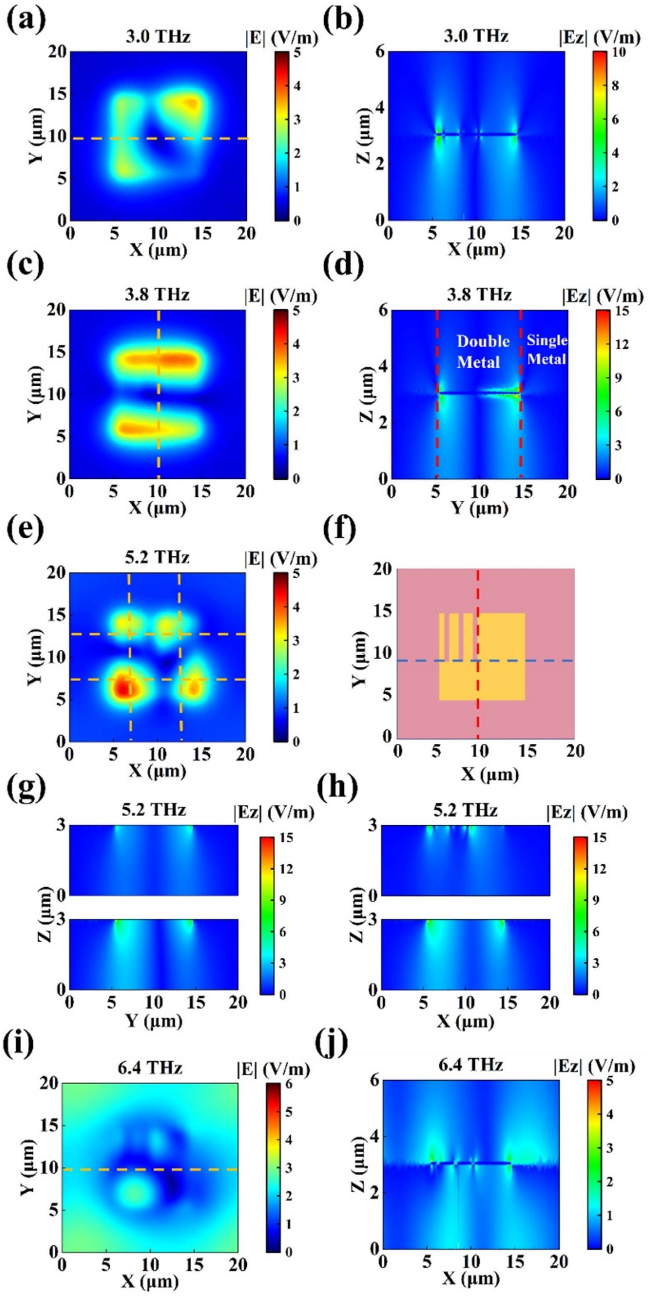

**Figure 2.** Spatial distribution of the electric field $|E|$ for one patch antenna unit (a) at 3.0 THz, (c) at 3.8 THz (e) at 5.2 THz, (i) at 6.4 THz in the $x$–$y$ plane at $z = 2$ $\mu$m. Spatial distribution of the electric field component $|E_z|$ at the cross-section plane denoted by the yellow dotted line (b) at 3.0 THz, (d) at 3.8 THz, (g) and (h) at 5.2 THz, (j) at 6.4 THz. The order of cavity resonance mode is denoted by the number of minima of the standing pattern of $|Ez|$. (f) Red dotted line divides the patch antenna into the right and left parts along the slot in $y$-direction, the blue dotted line divides the patch antenna into the top and bottom parts in the $x$-direction.

the electric field $|E_z|$ distribution of the central section in the $y$–$z$ plane of the left and right parts of the patch. The electric field $|E_z|$ of the first-order resonance mode can be observed in both sections. Figure 2(h) is the electric field $|E_z|$ distribution of the central section in the $x$–$z$ plane of the top and bottom parts. In the bottom part, a first-order microcavity effect can be observed, and in the top part, no microcavity effect is observed. Thus, the coupling peak at 5.2 THz is the combined effect of the first-order resonance on the left and right sides along the $y$-direction and the first-order resonance at the bottom part along the $x$-direction. At 6.4 THz, it can be seen in figure 2(i) that the electric field $|E|$ concentrated around the entire patch. Figure 2(j) shows that the first-order microcavity response along the $x$-axis is generated under the right part of the patch. In addition, figures 2(i) and (j) show that in addition to the coupling resonance of the microcavity, there is also electric field propagating between the antennas, which is a typical pattern of surface plasmon polariton (SPP) [24].

Therefore, the E-shaped patch antenna exhibits the characteristics of broadband coupling enhancement in the THz band because the asymmetric geometry resulted from the three slots breaks the degeneration of the original first-order resonance mode in $x$ and $y$ directions (3.0 and 3.8 THz), and results in the first-order coupling mode along $y$-direction on the left and right part and first-order coupling mode along $x$-direction at the bottom part at 5.2 THz, and the first-order microcavity coupling mode along $x$-direction on the right part supplemented by SPP at 6.4 THz. The four coupling peaks are generated to achieve the effect of broadband coupling enhancement.

It can be seen that the E-shaped patch antenna shows a significant effect to improve the optical coupling efficiency in a wide band, due to the introduction of three slots to the square patch antenna which demonstrates a narrow band effect in contrast. To understand the influence of slots, the effect of the related parameters of the slot, including the number of slots $n$, the width $w$, the length $g$, the distance between each slot $a$, and the distance from the first slot to the left antenna edge $m$, should be analyzed carefully. In the following simulation, we will study the effect of a given parameter on the coupling efficiency one by one when other parameters are fixed as $w = 0.5$ $\mu$m, $a = 1.5$ $\mu$m, $g = 5$ $\mu$m and $m = 0.5$ $\mu$m, and $n = 3$. Considering the requirement of broadband effect and high coupling efficiency, $n = 3$ is preferred. The change of $a$ has little effect on the peak position and intensity of the coupling efficiency when $a$ varies from 0.5 to 3 $\mu$m. It is also the case for $w$ and $m$, when $w$ varies from 0.5 to 3 $\mu$m and $m$ varies from 0.5 to 4 $\mu$m. The slot length $g$ would influence the spectral range and the intensity of the coupling efficiency. The position of the first peak shows a redshift with $g$ varying from 1 to 5 $\mu$m. When $g = 5$ $\mu$m, four coupling peaks can be observed. Considering the requirement of the broadest effect and the most uniform distribution, we selected the parameters to be $n = 3$, $w = 0.5$ $\mu$m, $a = 1.5$ $\mu$m, $g = 5$ $\mu$m, $m = 0.5$ $\mu$m in the following discussion.

In addition to the slot, the patch size will influence the coupling efficiency either. In figure 3, the effect of $S$ and $P$ on the coupling efficiency is investigated. Figure 3(a) shows the coupling efficiency of EAM-HIWIP with different $S$ when $L = 9$ $\mu$m, $P = 20$ $\mu$m. There are four peaks in 2.1–7.3 THz, the second and third peaks are redshift as $S$ increases. $S$ is the size along the $y$-direction. Figures 2(d) and (g) show the electric field distribution $|E_z|$ of second and third peaks along the $y$-direction. The change of $S$ leads to the variation of the length of the microcavity. According to equation (6), the

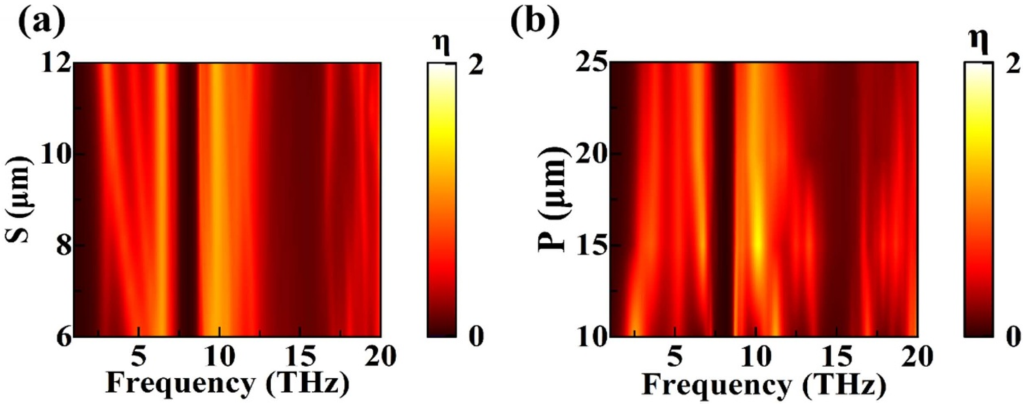

**Figure 3.** The dependence of the coupling efficiency of EAM-HIWIP on (a) S. (b) P.

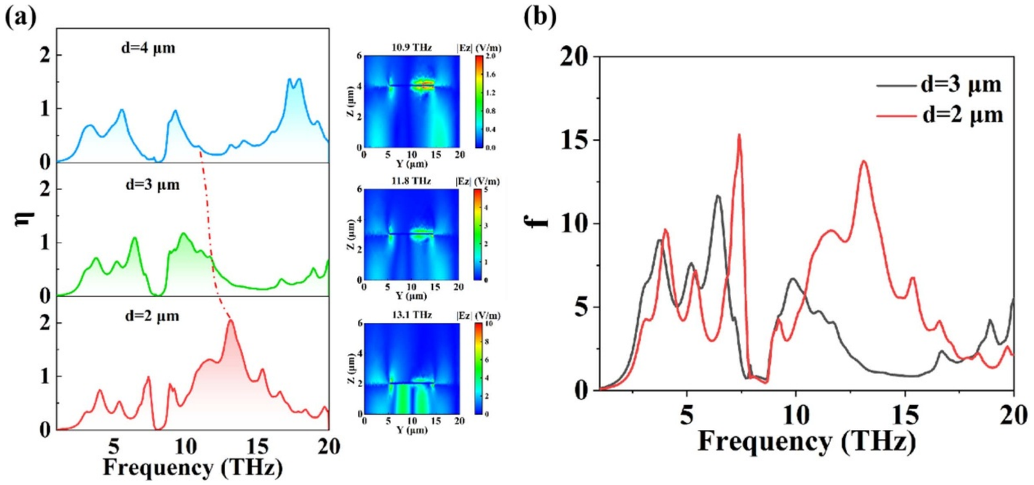

**Figure 4.** (a) The coupling efficiency of EAM-HIWIP with $S = 9\ \mu$m, $P = 20\ \mu$m and different $d$. The spatial distribution of electric field component $|E_z|$ in cross-section $y$–$z$ plane at 10.9 THz for $d = 4\ \mu$m, 11.8 THz for $d = 3\ \mu$m, 13.1 THz for $d = 2\ \mu$m. (b) The enhancement factor f of EAM-HIWIP in 1–20 THz with $d = 3\ \mu$m and $d = 2\ \mu$m.

relationship between $S$ and resonance frequency is a negative correlation, which means when $S$ increases the second and third peaks will redshift. Similarly, figures 2(b) and (j) show that the electric fields $|E_z|$ of the first and fourth peaks are distributed along the $x$-direction, which means the first and fourth peaks will not change as $S$ increases. The coupling efficiency of 8.6–12 THz is continuously and uniformly distributed, showing good broadband characteristics. The position of four peaks in 2.1–7.4 THz is most uniform in $S = 9\ \mu$m, therefore when $S = L = 9\ \mu$m the EAM-HIWIP has the best broadband performance with $P = 20\ \mu$m. Figure 3(b) shows the coupling efficiency with different period P when the antenna size $S = L = 9\ \mu$m. It is known in the case of a squared patch antenna, the period $P$ has little influence on the resonance frequency but mainly affects the magnitude of coupling efficiency [42]. In contrast, for the E-shaped patch antenna, the influence of period is more complicated. A smaller period is helpful to extend spectral coverage to lower frequency because the coupling between neighboring antennas increases. Nevertheless, the uniformity of the coupling enhancement degrades. When the period is larger than 15 $\mu$m, the coupling efficiency becomes more uniform and the effect of the period on the coupling efficiency is less obvious. Therefore, to design a suitable antenna, the choice of the period depends on the actual requirement. Considering the uniformity of the broadband effect and the coupling efficiency, $P = 20\ \mu$m is selected as the parameter for subsequent discussion.

Figure 4(a) gives the simulation results of the coupling efficiency of EAM-HIWIP with different $d$ when $S = 9\ \mu$m, and $P = 20\ \mu$m. It can be seen that the peak position shifts to low frequency gradually as the thickness increases from 2 to 4 $\mu$m. The coupling efficiency decreases with the thickness increases, which is especially obvious for the peak at 13.1 THz, as pointed out by the red dotted line in figure 4(a). This is because under the same incident light, the larger volume of the active region leads to lower the energy density. To illustrate the reason, the electric field distributions at 13.1, 11.8, and 10.9 THz for a thickness of 2, 3, and 4 $\mu$m are presented on the right of figure 4(a). When $d = 2\ \mu$m, the electric field propagating between the antennas and a third-order microcavity resonance feature can be seen clearly, so the coupling peak at 13.1 THz is due to the third-order microcavity resonance with supplement by SPP. The electric field of the microcavity effect gradually weakens with the

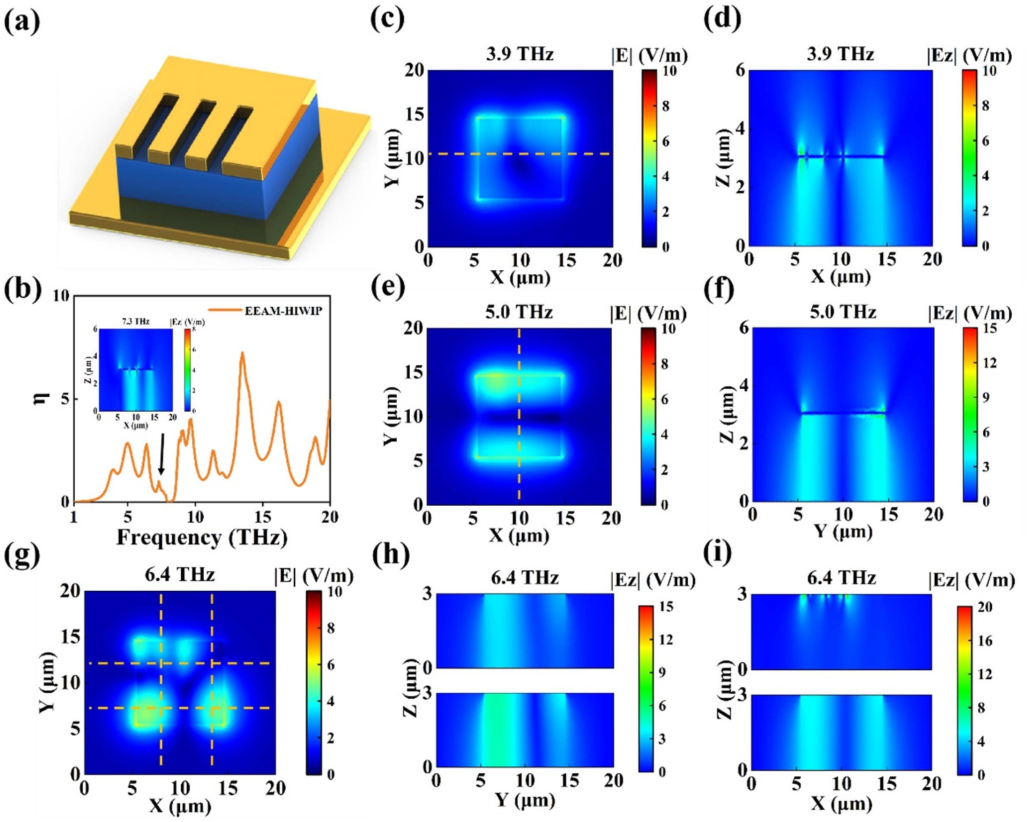

**Figure 5.** (a) The schematic of one unit of EEAM-HIWIP. (b) The coupling efficiency of EEAM-HIWIP with $S = 9$ $\mu$m, $P = 20$ $\mu$m, $d = 3$ $\mu$m. The inset shows the electric distribution $|E_z|$ in $x$–$z$ plane at 7.3 THz. Spatial distribution of the electric field |E| (c) at 3.9 THz, (e) at 5.0 THz, (g) at 6.4 THz in $x$–$y$ plane at $z = 2$ $\mu$m. Spatial distribution of the electric field component $|E_z|$ at the cross-section denoted by the yellow line for (d) 3.9 THz, (f) 5.0 THz, (h) and (i) 6.4 THz.

increase of thickness, leading to the coupling efficiency gradually decreases. At the same time, it can be seen that the peak at 13.1 THz not only reduces the coupling efficiency but also appears red-shifted. When the thickness of the active region increases, the effective refractive index of GaAs microcavity will increase, so the microcavity coupling peak shows a redshift. To sum up, the redshift combined with the decrease of the coupling peak at 13.1 THz result in a gradual weakening of the broadband enhancement feature of the EAM-HIWIP with increasing thickness. Figure 4(b) shows enhancement factors of the coupling efficiency from 1–20 THz. It can be seen that except for the Reststrahlen band, EAM-HIWIP has a broadband coupling enhancement effect in the THz band. Especially in 2–5 THz where the high-performance THz source (THz QCL) usually performs, such an E-shaped patch antenna demonstrates a significant effect, and theoretically improves the coupling efficiency over five times, which is meaningful for many potential applications such as THz imaging etc. Compared with the reference HIWIP with $d = 3$ $\mu$m, the highest coupling efficiency is increased by a factor of 11 at 6.4 THz. Since the overall coupling efficiency of the device increases with the thickness of the active region, the enhancement factor at $d = 2$ $\mu$m is calculated and plotted in figure 4(b) for comparison. The enhancement factor is larger at $d = 2$ $\mu$m than at $d = 3$ $\mu$m, the highest coupling efficiency could be as high as 15 at 7.4 THz. The high coupling efficiency indicates that equivalent responsivity could be obtained with a thinner device.

### 3.2. *EEAM-HIWIP*

To further improve the performance, the EEAM-HIWIP structure is introduced, in which the part of the active region except the antenna covered is etched away. Figure 5(a) shows the schematic of one unit of EEAM-HIWIP. Because the etched structure reduces the area of the device, the dark current can be effectively reduced [45]. The broadband coupling enhancement effect of EEAM-HIWIP is analyzed and discussed. Figure 5(b) shows the coupling efficiency of EEAM-HIWIP in 1–20 THz. Similar to EAM-HIWIP, we focus on the coupling peaks located below the Reststrahlen band. Three strong coupling peaks at 3.9, 5.0, and 6.4 THz and a weak peak at 7.3 THz below the Restrahlen band can be observed in figure 5(b). The electric field distributions at the coupling peaks for EEAM-HIWIP are given in figure 5. It can be seen that the electric field distributions of the three coupling peaks generated in EEAM-HIWIP (figures 5(c), (e) and (g)) are similar to that of EAM-HIWIP (figures 2(a), (c) and (e)). In EEAM-HIWIP, the coupling peak at 3.9 and 5.0 THz is due to the first-order microcavity coupling along

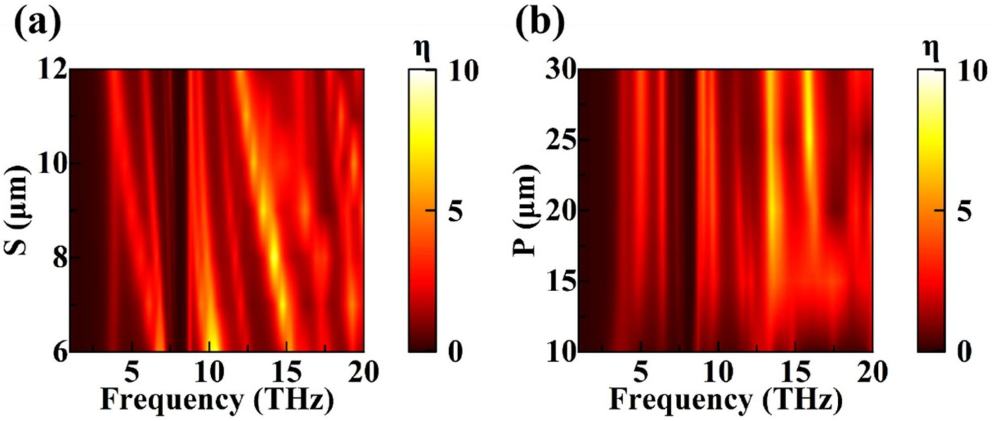

**Figure 6.** (a) The dependence of the coupling efficiency of EEAM-HIWIP on $S$ when $P = 20$ $\mu$m, $d = 3$ $\mu$m. (b) The dependence of the coupling efficiency of EEAM-HIWIP on P with $S = 9$ $\mu$m, $d = 3$ $\mu$m.

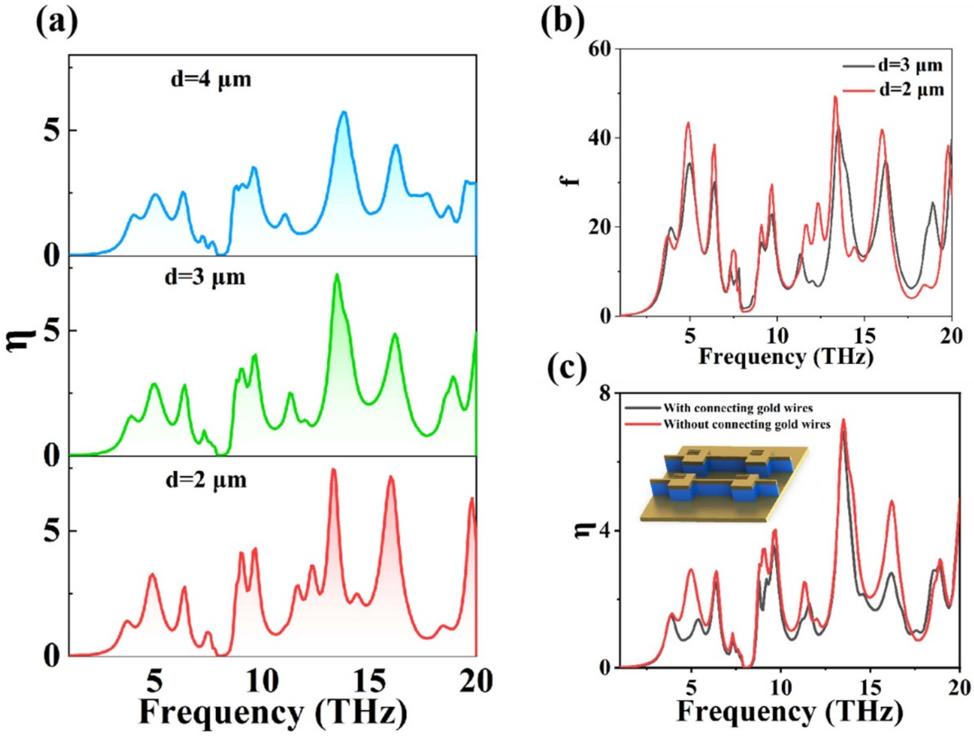

**Figure 7.** (a) The coupling efficiency of EEAM-HIWIP for different $d$ when $S = 9$ $\mu$m, $P = 20$ $\mu$m. (b) The enhancement factor of EEAM-HIWIP for $d = 3$ $\mu$m and $d = 2$ $\mu$m when $S = 9$ $\mu$m, $P = 20$ $\mu$m. (c) The comparison of coupling efficiency for EEAM-HIWIP with and without connecting gold wires.

the $x$-direction and the $y$-direction, respectively. The coupling peak at 6.4 THz is due to the joint interaction of the first-order microcavity coupling modes generated by the left and right parts of the patch antenna along the $y$-direction and the bottom part along the $x$-direction. The electric field distribution of the fourth weak coupling peak at the 7.3 THz is presented in figure 5(b) inset. Because SPP mode is suppressed in the etched structure, the coupling efficiency is relatively weak, which is different from the case of EAM-HIWIP at 6.4 THz in figure 2(j). In contrast, the coupling efficiencies of the other three peaks are significantly enhanced.

Figure 6(a) shows the dependence of the coupling efficiency on $S$ when $P = 20$ $\mu$m, $d = 3$ $\mu$m, and $L = 9$ $\mu$m. Similar to the case of EAM-HIWIP, there are three distinct coupling peaks below the Reststrahlen band, and the second and third peaks redshift with the increase of $S$. Figure 6(b) is the variation of coupling efficiency with different $P$ for $S = L = 9$ $\mu$m and $d = 3$ $\mu$m. It can be seen that when the period of EEAM-HIWIP is larger than 20 $\mu$m, it has less influence on the coupling efficiency.

Figure 7(a) shows the coupling efficiency of EEAM-HIWIP as a function of $d$ at $S = 9$ $\mu$m and $P = 20$ $\mu$m. Similar to the case of EAM-HIWIP, the coupling efficiency

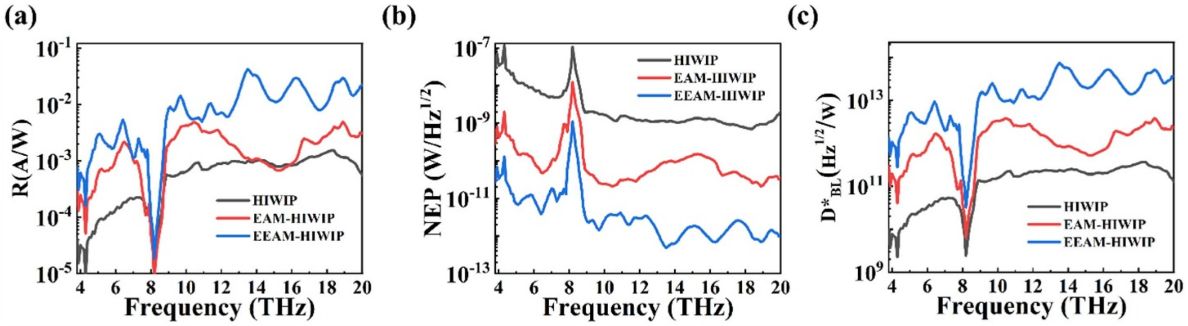

**Figure 8.** (a) The responsivity R(A/W) of HIWIP, EAM-HIWIP and EEAM-HIWIP. (b) NEP(W/Hz$^{1/2}$) of HIWIP, EAM-HIWIP and EEAM-HIWIP. (c) D$^*$(Hz$^{1/2}$/W) of HIWIP, EAM-HIWIP and EEAM-HIWIP.

of EEAM-HIWIP decreases with increasing thickness. Compared with EAM-HIWIP, the coupling efficiency of EEAM-HIWIIP is significantly improved, because the active region outside the antenna is etched away, the volume of the active region becomes smaller, so the energy density under each antenna will become larger [24]. Figure 7(b) shows the enhancement factor of EEAM-HIWIP with different thickness *d*. It can be seen in figure 7(b) that EEAM-HIWIP has a broadband enhancement effect from 2.3 to 20 THz. Compared with the reference HIWIP with $d = 3$ μm, the coupling efficiency is 19 times at 3.9 THz, 34 times at 5.0 THz, 30 times at 6.4 THz, and 15 times on average at 2.3–20 THz, respectively. The coupling efficiency of the device is improved by one order of magnitude. As the thickness of the active region decreases, the enhancement factor increases, which means that EEAM-HIWIP has the potential to acquire comparable responsivity with reduced thickness. In reality, etched patch antennas should be electrically connected by metal strips, as shown in the inset of figure 7(c). With connecting gold wires, the broadband enhancement effect is still obvious but the coupling efficiency is slightly reduced.

To better understand the performance of the broadband detector, the responsivity R, noise equivalent power NEP, and specific detectivity D$^*$ of EAM-HIWIP and EEAM-HIWIP are calculated and shown in figure 8. The p-GaAs HIWIP is chosen as the reference sample [16, 17, 36]. The responsivity, NEP, and specific detectivity of the reference sample are denoted as R$_0$, NEP$_0$, and $D_0^*$. The responsivity is the experimental result measured at a bias of 0.2 V for $T = 3.4$ K [16]. $NEP_0 = i_d/R_0$, $i_d$ is the dark current. Specific detectivity $D_0^* = A_0^{\frac{1}{2}}/NEP_0$ $A_0 = 6.76\times10^4$ μm$^2$ is the area of the photodetector. According to the measured responsivity, the dark current $i_d$ as well as the area of HIWIP photodetector, R$_0$, NEP$_0$, and $D_0^*$ of the HIWIP is obtained accordingly, which are displayed in black lines in figure 8. To demonstrate the effect of E-shaped patch antenna, the detector performance of both EAM-HIWIP and EEAM-HIWIP with 16 unit cells ($L$ = S = 9 μm, $P$ = 20 μm) is calculated, whose photodetector area are $A_{EAM} = 6400$ μm$^2$ and $A_{EEAM} = 1296$ μm$^2$, respectively. Based on the estimated relationship $R_{EAM/EEAM} = R_0 \times f$, $NEP_{EAM/EEAM} = \frac{A_{EAM/EEAM}}{A_0} \times \frac{1}{f} \times NEP_0$, $D^*_{EAM/EEAM} = \frac{\sqrt{A_{EAM/EEAM}}}{NEP_{EAM/EEAM}}$ [20, 24], the R, NEP, and D$^*$ of EAM-HIWIP and EEAM-HIWIP are calculated and the corresponding results are plotted in figure 8. Both structures show a significant broadband enhancement effect. The responsivity of EAM-HIWIIP is one order of magnitude higher than HIWIP at 3.8–12 THz. The responsivity of EEAM-HIWIP is double that of EAM-HIWIP. The NEP of three devices is plotted in figure 8(b), the EAM-HIWIP and the EEAM-HIWIP can decrease the NEP by nearly two and three orders of magnitude at 3.8–20 THz, respectively. And the specific detectivity of EAM-HIWIP and EEAM-HIWIP is one and two orders of magnitude higher than that of HIWIP, respectively. The high specific detectivity and low dark current make it possible to realize a higher operating temperature for the THz broadband detector with such an E-shaped patch antenna microcavity structure.

## 4. Conclusion

In this paper, we propose an E-shaped patch antenna microcavity structure to improve the performance of THz broadband detectors. The GaAs-based broadband HIWIP is used as an example to study the effect of the E-shaped patch antenna structure. Two kinds of geometry, i.e. the EAM-HIWIP and EEAM-HIWIP are simulated. In the EAM-HIWIP, due to the introduction of the three slots, the first-order microcavity coupling modes in the *x* and *y* direction, which are originally degenerate in the square patch antenna, split into two peaks at 3.0 and 3.8 THz, and new coupling modes at 5.2 and 6.4 THz are generated simultaneously. The split of degenerated modes and the excitation of multiple microcavity modes as well as SPP lead to the broadband enhancement effect on the detector in the THz range. The effect of the slots is analyzed. By adjusting the width *S* and the period *P*, the coupling frequency, and the coupling efficiency could be optimized. The thickness *d* of the active region is inversely proportional to the coupling efficiency. The thinner the device, the better the broadband enhancement effect can be exhibited. Compared with the reference HIWIP, the coupling efficiency of EAM-HIWIP is improved by four times. The device performance can be further improved by EEAM-HIWIP which could reduce the dark current besides achieving broadband enhancement of coupling efficiency. By adjusting *S*, *P*, and *d*, the coupling efficiency of EEAM-HIWIP could be improved by 15 times. The theoretical calculation shows that the EAM-HIWIP and EEAM-HIWIP can effectively improve the responsivity, NEP, and specific detectivity. For EEAM-HIWIP, the responsivity increased by one order of magnitude. The specific detectivity can be increased by two orders of magnitude. The NEP decreased by three orders of magnitude. The high specific detectivity and low dark current make it possible to realize a higher operating temperature. Both EAM-HIWIP and EEAM-HIWIP effectively enhance the broadband response of HIWIP, revealing their great potential for application in THz broadband detection. The present design scheme provides a guideline to realize high-performance THz broadband detection, which could also be applied to other THz broadband photodetectors, such as the BIB detector or HEIWIP, etc.

## Data availability statement

The data that support the findings of this study are available upon reasonable request from the authors.

## Acknowledgments

This work was supported by the Natural Science Foundation of China (12074249, 12274285, 61974151, 61734006, 12104061, 11834011, and 61574149), Natural Science Foundation of Shanghai (20ZR1466200, 21ZR1474000), Project funded by China Postdoctoral Science Foundation (2020M680458), Open Project funded by Key Laboratory of Artificial Structures and Quantum Control (2020-03).

## ORCID iD

X R Lian https://orcid.org/0000-0003-3879-1779

## References

[1] Rogalski A and Sizov F 2011 Terahertz detectors and focal plane arrays *Opto-Electron. Rev.* **19** 346–404

[2] Xu W D, Xie L J and Ying Y B 2017 Mechanisms and applications of terahertz metamaterial sensing: a review *Nanoscale* **9** 13864–78

[3] Kleine-Ostmann T and Nagatsuma T 2011 A review on terahertz communications research *J. Infrared Millim. Terahertz Waves* **32** 143–71

[4] Bai P *et al* 2019 Broadband THz to NIR up-converter for photon-type THz imaging *Nat. Commun.* **10** 3513

[5] Bai P *et al* 2021 Ultra-broadband THz/IR upconversion and photovoltaic response in semiconductor ratchet-based upconverter *Appl. Phys. Lett.* **119** 241104

[6] Eisele H, Naftaly M and Fletcher J R 2007 A simple interferometer for the characterization of sources at terahertz frequencies *Meas. Sci. Technol.* **18** 2623–8

[7] Simoens F 2014 THz bolometer detectors *Physics and Applications of Terahertz Radiation* ed M Perenzoni and D J Paul 173 (New York: Springer) pp 35–75

[8] Wang X D, Wang B B, Hou L W, Xie W, Chen X Y and Pan M 2015 Design consideration of GaAs-based blocked-impurity-band detector with the absorbing layer formed by ion implantation *Opt. Quantum Electron.* **47** 1347–55

[9] Wang X D, Wang B B, Chen Y L, Hou L W, Xie W, Chen X Y and Pan M 2016 Spectral response characteristics of novel ion-implanted planar GaAs blocked-impurity-band detectors in the terahertz domain *Opt. Quantum Electron.* **48** 518

[10] Mittendorff M, Winnerl S, Kamann J, Eroms J, Weiss D, Schneider H and Helm M 2013 Ultrafast graphene-based broadband THz detector *Appl. Phys. Lett.* **103** 021113

[11] Castilla S *et al* 2019 Fast and sensitive terahertz detection using an antenna-integrated graphene PN junction *Nano Lett.* **19** 2765–73

[12] Cai Y J, Guo Y B, Zhang H Y, Wang Y, Chen C Y, Lin F, Zuo S K and Zhou Y G 2021 Tunable and polarization-sensitive graphene-based terahertz absorber with eight absorption bands *J. Appl. Phys.* **54** 195106

[13] He X W *et al* 2014 Carbon nanotube terahertz detector *Nano Lett.* **14** 3953–8

[14] Wang L *et al* 2017 Toward sensitive room-temperature broadband detection from infrared to terahertz with antenna-integrated black phosphorus photoconductor *Adv. Funct. Mater.* **27** 1604414

[15] Perera A G U 2016 Heterojunction and superlattice detectors for infrared to ultraviolet *Prog. Quantum Electron.* **48** 1–56

[16] Bai P, Zhang Y H, Guo X G, Fu Z L, Cao J C and Shen W Z 2018 Realization of the high-performance THz GaAs homojunction detector below the frequency of Reststrahlen band *Appl. Phys. Lett.* **113** 241102

[17] Perera A G U, Shen W Z, Liu H C, Buchanan M and Schaff W J 2000 GaAs homojunction interfacial workfunction internal photoemission (HIWIP) far-infrared detectors *Mater. Sci. Eng.* B **74** 56–60

[18] Matsik S G, Rinzan M B M, Perera A G U, Liu H C, Wasilewski Z R and Buchanan M 2003 Cutoff tailorability of heterojunction terahertz detectors *Appl. Phys. Lett.* **82** 139–41

[19] Palaferri D *et al* 2018 Room-temperature nine-mu m-wavelength photodetectors and GHz-frequency heterodyne receivers *Nature* **556** 85

[20] Cheng Y Q *et al* 2020 Strongly enhanced local electromagnetic field in mid-infrared and terahertz photodetectors employing a hybrid antenna *AIP Adv.* **10** 015048

[21] Shao D X, Zhang R, Fu Z L, Guo X G, Zhuang S L and Cao J C 2019 High responsivity random metal grating couplers for terahertz quantum well photodetectors *Semicond. Sci. Technol.* **34** 075029

[22] Zhang R, Shao D X, Fu Z L, Wang H X, Zhou T, Tan Z Y and Cao J C 2017 Terahertz quantum well photodetectors with metal-grating couplers *IEEE J. Sel. Top. Quantum Electron.* **23** 3800407

[23] Yachmenev A E, Khabibullin R A and Ponomarev D S 2022 Recent advances in THz detectors based on semiconductor structures with quantum confinement: a review *J. Appl. Phys.* **55** 193001

[24] Bai X Q, Bai P, Li X H, Huang S H, Lian X R, Song W J, Shi Z W, Shen W Z and Zhang Y H 2021 Optical coupling enhancement of multi-color terahertz quantum well detector *J. Appl. Phys.* **130** 203102

[25] Palaferri D, Todorov Y, Chen Y N, Madeo J, Vasanelli A, Li L H, Davies A G, Linfield E H and Sirtori C 2015 Patch antenna terahertz photodetectors *Appl. Phys. Lett.* **106** 161102

[26] Deshmukh A A and Ray K P 2009 Compact broadband slotted rectangular microstrip antenna *IEEE Antennas Wirel. Propag. Lett.* **8** 1410–3

[27] Borchardt J J and Lapointe T C 2019 U-slot patch antenna principle and design methodology using characteristic

mode analysis and coupled mode theory *IEEE Access* **7** 109375–85

[28] Ooi B L and Shen Q 2000 A novel E-shaped broadband microstrip patch antenna *Microw. Opt. Technol. Lett.* **27** 348–52

[29] Deshmukh A A, Singh D and Ray K P 2019 Modified designs of broadband E-shape microstrip antennas *Sadhana-Acad. Proc. Eng. Sci.* **44** 64

[30] Katyal A and Basu A 2017 Compact and broadband stacked microstrip patch antenna for target scanning applications *IEEE Antennas Wirel. Propag. Lett.* **16** 381–4

[31] Cao Y F, Cai Y, Cao W Q, Xi B K, Qian Z P, Wu T and Zhu L 2019 Broadband and high-gain microstrip patch antenna loaded with parasitic mushroom-type structure *IEEE Antennas Wirel. Propag. Lett.* **18** 1405–9

[32] Wang B-X, Tang C, Niu Q S, He Y H and Chen R Y 2019 A broadband terahertz metamaterial absorber enabled by the simple design of a rectangular-shaped resonator with an elongated slot *Nanoscale Adv.* **1** 3621–5

[33] Bhardwaj S and Rahmat-Samii Y 2012 A comparative study of c-shaped, e-shaped, and u-slotted patch antennas *Microw. Opt. Technol. Lett.* **54** 1746–57

[34] Yu G, Zhang Y H and Shen W Z 2002 Far-infrared spectroscopic study of GaAs multi-layer n(+)-i structures *Appl. Surf. Sci.* **199** 160–5

[35] Esaev D G, Rinzan M B M, Matsik S G and Perera A G U 2004 Design and optimization of GaAs/AlGaAs heterojunction infrared detectors *J. Appl. Phys.* **96** 4588–97

[36] Shen W Z, Perera A G U, Liu H C, Buchanan M and Schaff W J 1997 Bias effects in high performance GaAs homojunction far-infrared detectors *Appl. Phys. Lett.* **71** 2677–9

[37] Perera A G U, Matsik S G, Jayaweera P V V, Tennakone K, Liu H C, Buchanan M, Von Winckel G, Stintz A and Krishna S 2006 High operating temperature split-off band infrared detectors *Appl. Phys. Lett.* **89** 131118

[38] Dey S and Mittra R 1999 A conformal finite-difference time-domain technique for modeling cylindrical dielectric resonators *IEEE Trans. Microw. Theory Tech.* **47** 1737–9

[39] Li L J, Bai P, Zhang Y C, Shen W Z and Cao J C 2018 Optical field simulation of edge coupled terahertz quantum well photodetectors *AIP Adv.* **8** 035214

[40] Liu L, Chen Y, Huang Z, Du W, Zhan P and Wang Z L 2016 Highly efficient metallic optical incouplers for quantum well infrared photodetectors *Sci. Rep.* **6** 30414

[41] Esaev D G, Matsik S G, Rinzan M B M, Perera A G U, Liu H C and Buchanan M 2003 Resonant cavity enhancement in heterojunction GaAs/AlGaAs terahertz detectors *J. Appl. Phys.* **93** 1879–83

[42] Todorov Y, Tosetto L, Teissier J, Andrews A M, Klang P, Colombelli R, Sagnes I, Strasser G and Sirtori C 2010 Optical properties of metal-dielectric-metal microcavities in the THz frequency range *Opt. Express* **18** 13886–907

[43] Guo X G, Zhang R, Cao J C and Liu H C 2012 Numerical study on metal cavity couplers for terahertz quantum-well photodetectors *IEEE J. Quantum Electron.* **48** 728–33

[44] Chen Y N 2015 Antenna coupled quantum infrared detectors

[45] Chen Y N, Todorov Y, Askenazi B, Vasanelli A, Biasiol G, Colombelli R and Sirtori C 2014 Antenna-coupled microcavities for enhanced infrared photo-detection *Appl. Phys. Lett.* **104** 031113